Slot-Die Coating Operability Window for Nanoparticle Bed Deposition in a Microscale Selective Laser Sintering Tool

Dipankar Behera

The University of Texas at Austin, Austin, TX 78712

Daniel Liao

The University of Texas at Austin, Austin, TX 78712

Michael A. Cullinan¹

The University of Texas at Austin,
Austin, TX 78712

e-mail: michael.cullinan@austin.utexas.edu

This work seeks to develop a fundamental understanding of slot-die coating as a nanoparticle bed deposition mechanism for a microscale selective laser sintering (μ-SLS) process. The specific requirements of the μ-SLS process to deposit uniform sub-5 μm metal nanoparticle films while enabling high throughput fabrication make the slot-die coating process a strong candidate for layer-by-layer deposition. The key challenges of a coating system are to enable uniform nanoparticle ink deposition in an intermittent layer-bylayer manner. Identifying the experimental parameters to achieve this using a slot-die coating process is difficult. Therefore, the main contribution of this study is to develop a framework to predict the wet film thickness and onset of coating defects by simulating the experimental conditions of the μ -SLS process. The single-layer deposition characteristics and the operational window for the slot-die coating setup have been investigated through experiments and two-dimensional computational fluid dynamics simulations. The effect of coating parameters such as inlet speed, coating speed, and coating gap on the wet film thickness has been analyzed. For inlet speeds higher than the coating speed, it was found that the meniscus was susceptible to high instabilities leading to coating defects. Additionally, the study outlines the conditions for which the stability of the menisci upstream and downstream of the slot-die coater can affect the uniformity and thickness range of *the coating.* [DOI: 10.1115/1.4049668]

1 Introduction

According to ASTM F42 standards, additive manufacturing (AM) is defined as the "process of joining materials" in a layer-bylayer manner to make three-dimensional (3D) objects from digital design data as opposed to subtractive manufacturing methodologies [1]. The innovations in design automation and optimization have opened a plethora of complex yet multifunctional designs with considerations for strong and lightweight structures, optimized material usage, improved structural and electrical properties. Therefore, at its core, the fundamental value addition of AM lies in its ability to deposit and consolidate material in a layer-bylayer manner, thereby enabling fabrication of complex geometries [2,3]. Most industrial applications of commercial AM machines have been targeted toward rapid prototyping of noncritical and customized parts in the automotive [4], aerospace [5], and biomedical [6] sectors. A leading area of research in AM community is to leverage the design independence afforded by AM for fabrication of microscale geometries with applications in semiconductor, micro-electromechanical systems/micro-opto-electromechanical systems, and medical devices industries. While the initial interest in AM as a micromanufacturing process was generated with the advent of microstereolithography, it was limited by photopolymerizable materials. A potential application of microscale AM is in the fabrication of wafer-scale metallic interconnects in microelectronics packaging, currently achieved using a combination of lithography, and electroplating and etching techniques. However, most commercially available metal AM machines have a resolution limit of around 50 μ m, preventing them from expanding into the micro-electronics packaging sector where sub-10 μ m features are critical [7]. Micromanufacturing techniques included in backend-of-line semiconductor processes (including IC packaging) are

severely limited by the geometric and design constraints, thereby introducing scalability issues. Furthermore, with the constant demand for miniaturization, there has been a gradual shift into codesigning 3D chips with geometric and functional requirements. This is where microscale AM processes capable of fabricating true-3D metallic parts become important. One recently proposed way to address this gap through the development of a microscale selective laser sintering (μ -SLS) process is designed to fabricate true-3D metallic parts with a resolution of 1 μ m [7–10].

1.1 Brief Introduction to μ -Selective Laser Sintering. The basic working principle of μ -SLS revolves around same ideas encompassed by conventional SLS [2,11]. In this process, a 3D geometry is divided into several two-dimensional (2D) layers using a slicing software. After that, a material bed is deposited on the substrate to form the first layer. The laser then selectively scans across the material bed to fuse together the particles in the first layer. After the first layer is sintered, the next layer of material is deposited on top of it, followed by selective sintering using the laser. The process is repeated until all the sliced layers of the 3D geometry are deposited on top of each other to form the part. Excess material is then removed to obtain the 3D part. The key requirements of the μ -SLS system are to obtain true-3D geometries with a resolution of 1 μ m and provide a part fabrication throughput comparable to those of other back-end-of-line processes. To achieve this, the μ -SLS system has three main subsystems deposition mechanism, optical subsystem, and the translation subsystem to move and align the substrate between under the deposition and optical subsystems, the detailed design and integration of which have been discussed in previous works [7,12,13].

1.2 Material Considerations and Bed Deposition Mechanism Selection for μ -Selective Laser Sintering. Typical powder bed fusion (PBF) processes like selective laser sintering and selective laser melting targeted toward metal part fabrication use discrete solid-state mesoscale and microscale powders as the starting

¹Corresponding author.

Contributed by the Manufacturing Engineering Division of ASME for publication in the JOURNAL OF MICRO- AND NANO-MANUFACTURING. Manuscript received July 19, 2020; final manuscript received December 16, 2020; published online February 1, 2021. Assoc. Editor: Ping Guo.

material. A uniform and narrow particle size distribution ensures a high-quality sintering. There are three widely incorporated bed deposition mechanisms in PBF processes—laser powder bed, e.g., SLS, laser powder fed, e.g., laser engineered net shaping, and binder jetting [2]. The typical powder spreading mechanisms for laser powder bed and binder jetting include depositing and spreading the layers using rollers [14,15], while laser powder fed processes use an air-blown nozzle to deposit powders [16].

One of the key requirements for the μ -SLS process is to achieve a feature size resolution of $1 \mu m$, which means that the discrete material to be used needs to be at least an order of magnitude smaller than the resolution. Therefore, nanoparticle-based (NPs) powders need to be used for fabricating microscale parts of the desired resolution. However, a significant disadvantage of NPs is the high surface area-to-volume ratio due to which they tend to agglomerate and reduce the effective surface energy of the system [9,17]. Additionally, NPs are susceptible to oxidation and thus, they need to be processed under high vacuum systems. Therefore, nanoparticles suspended in a solvent are critical to avoid the issues associated with agglomeration and oxidation. Roy et al. studied the compatibility of Cu nanoscale powders and nanoparticle inks (NP inks) for the μ -SLS process and investigated effect of particle size and morphology to ensure uniform sintering characteristics [18]. A concurrent study by Roy et al. determined the most optimal laser parameters for the ensuring good sintering characteristics [19]. Based on these findings, Cu and Ag NP inks were identified, which exhibit good sintering characteristics compatible with an near infrared-continuous wave laser.

The most efficient way of designing a solution analogous to PBF methods for deposition of NP inks was to use a film-forming technique. The main requirements for selecting the bed deposition method for μ -SLS are as follows—(1) Enable layer-by-layer deposition of thin films, (2) Ensure sub-5 μ m deposition thickness, (3) Target uniform deposition thickness, (4) Ensure uniform thickness after layer-by-layer deposition, (5) Reduce material wastage, (6) High throughput capabilities, and (7) Deposit wide range of material rheology.

1.3 Selection of Film-Forming Method. The most comprehensive usage of film forming techniques at the dimension scales targeted for the μ -SLS process has been explored in the batteries and photovoltaic cells industry [20,21]. These methods can be categorized based on single substrate implementation and roll-toroll (R2R) implementation. Single substrate printing and coating techniques involve processes like casting, spin coating, doctorblading, screen-printing, ink-jet printing, and pad-printing. In contrast to these single substrate techniques, R2R coating techniques include processes like knife-over edge printing, slot-die coating, gravure coating, curtain coating, and slide coating. It must be noted that all these processes have a significant dependence on the process parameters and material rheology, and are generally validated by the resulting thicknesses, film morphology, and surface topography.

While keeping the requirements of the μ -SLS deposition mechanism in mind, and evaluating some of the available film forming techniques, the following insights are necessary. Spin coating is an extensively researched and implemented technique in several industries including micro-electronics and allows for the formation of highly homogenous films with a wide range of coating thicknesses. The basic setup of a spin coating process is straightforward where a solution is applied on a rotating substrate. The angular velocity of the substrate leads to the ejection of most of the liquid and only a thin film is left on the substrate. The resulting film characteristics depend on the angular velocity, molecular weight, solute concentration, viscosity, volatility, and diffusivity of the solution. While the process is highly reproducible and can produce sub-1 um films, most of the applied liquid is ejected during the process, leading to high material wastage [22]. Moreover, the integration of a spin coating technique for layer-by-layer fabrication without perturbing the deposited and sintered layers makes it difficult to implement the process for high throughput μ -SLS process.

Doctor blading (R2R analogous is called knife-over edge coating) uses a sharp edge to linearly spread the coating solution from a reservoir in front of it [23]. The process produces uniform single layer films without significant material wastage, but it has been shown to repeatably produce films down to $20\,\mu\text{m}$. Screen printing uses a 'squeegee' to push the coating solution on the substrate under contact. However, it requires highly viscous material and the associated wet film thicknesses achieved using this process are high (> $10\,\mu\text{m}$) [24], which would not work well for the μ -SLS process.

Inkjet printing has been primarily developed for office printing applications, but over the last decade, it has been a leading candidate for droplet deposition in printed electronics and microfabrication processes. The droplets are typically formed using mechanical compression (pneumatic, ultrasonic or piezo-electric actuation) or thermally creating a pressure differential [25,26]. The droplet is then electrostatically charged and deposited on the substrate at high speeds. However, the process is typically limited to low viscosity, high surface tension inks, and needs to have codesigned inks for uniform droplet placement. Although the process is more suited for complex deposition patterns, from the perspective of μ -SLS, the need to have an accurate control over the inkjet and process parameters, small print areas, and need for parallelization of inkjet heads make it challenging.

Gravure coating uses a two-roller system to transfer the ink to the substrate and is typically designed for R2R systems only [27,28]. Slot-die coating is premetered coating technique that deposits all the liquid that is pushed through a thin slot formed between two precise die heads on to the substrate [29]. This process can attain ultrathin (\sim 1 μ m) film thicknesses for a wide range of material viscosity over large areas, and uniformity is theoretically dependent on the flow rate of the fluid. However, the stability of the coating meniscus defines the uniformity of the process and the steady-state thickness, and it is dependent on several parameters including substrate speed, die gap and coating gap, and the distance between the substrate and the die lips.

The compatibility of film-forming techniques for layer-by-layer thin film deposition for μ -SLS applications has been outlined in Table 1. As it can be seen, slot-die coating stands out as the best candidate for a high throughput, layer-by-layer deposition of sub-5 μ m NP ink films. Conventionally, slot-die coating has been explored in R2R systems. Furthermore, multilayer coatings using the slot-die coating process have been done in a simultaneous manner where two or more liquids are deposited at the same time through multiple slots. It must be noted that the mechanics of the μ -SLS process makes it a noncontinuous process (unlike R2R), which introduces additional challenges for intermittent and layer-by-layer slot-die coating.

1.4 Slot-Die Coating Process Mechanics and Literature Review. The fundamental ideas behind the slot-die coating process are derived from the Landau-Levich approximations of the film thickness of a liquid dragged by a moving plate [30,31]. In the slot-die coating process, the liquid enters a fixed gap slot encompassed by two (or more) precisely machined dies and exits the die to establish contact with the substrate. The coating gap is filled with liquid to establish the coating bead which is bound by the upstream and downstream menisci. After establishing the coating bead, the substrate is linearly translated to spread the liquid and form a film. The upper meniscus initiates the formation of the coating bead, while the lower meniscus facilitates the spreading process. Figure 1 outlines the coating bead formation process, followed by the filling of the coating gap with liquid as it contacts the substrate and spreading of the liquid due to substrate motion.

The operating limits of a slot-die coating process are bound by a range of parameters such as flow rate, coating gap, and coating

Table 1 Compatibility of film-forming methods for μ -SLS applications

Parameter	Spin coating	Doctor blading	Screen printing	Inkjet printing	Gravure coating	Slot-die coating
Viscosity range (cP) Film thickness (µm) Speed (mm/s) Intermittent Material wastage Scalability to wafers	<10 1-100 — + ++++	<10 5-100 <20 ++ +++	100-10,000 10-500 20-1500 ++ ++	<10 1–500 20–200 ++++ +	10–1000 5–100 200–5000 ++++ +	10–10,000 1–250 5–1000 +++ + +++

+: very difficult/very low, ++: difficult/low, +++: somewhat difficult/high, and ++++: simple/very high.

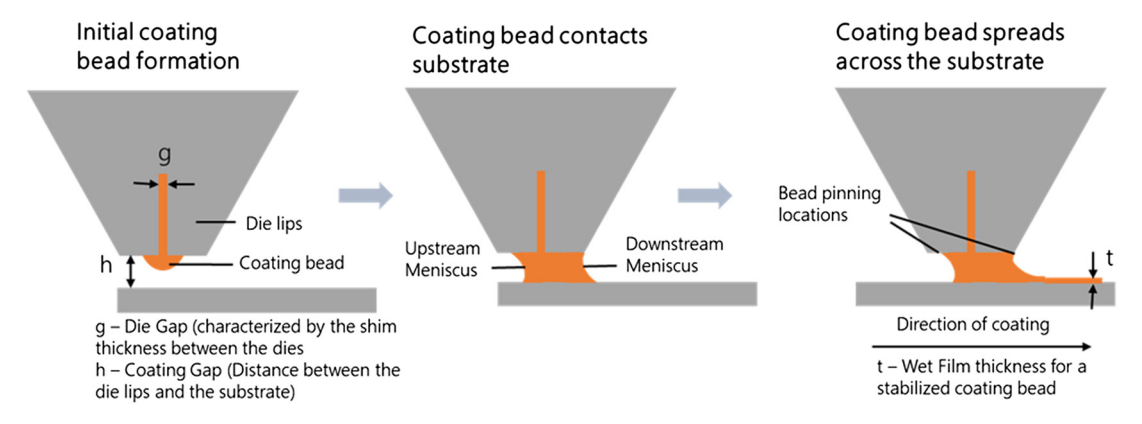


Fig. 1 General working principle of the slot-die coating process

speed. The operating range is defined as the range of parameters that yields films free of defects such as ribbing, air entrainment, and dripping [29,32]. Previous studies have established analytical models to determine the operating limits of the slot-die coating process with broad assumptions. Ruschak developed the capillary model that uses a vacuum pressure at the upstream slot die to control the meniscus pinning location [33]. The capillary model also assumes that viscous effects are small, and both the upstream and downstream meniscus are pinned at their respective slot-die edge. The operating limits are defined by

$$\frac{1 + \cos\theta}{h} + \frac{1.34 \text{Ca}^{2/3}}{t} \le \Delta P \le \frac{1 - \cos\theta}{h} + \frac{1.34 \text{Ca}^{2/3}}{t} \quad (1)$$

where ΔP represents the vacuum pressure between the upstream and downstream meniscus, σ is a constant liquid surface tension, h is the coating gap, t is the film thickness. The minimum film thickness for a system without vacuum pressure can be determined from inequality Eq. (2) by setting the lower bound to zero

$$t = \frac{1.34 \text{Ca}^{2/3}}{t} \frac{h}{1 + \cos\theta}$$
 (2)

The viscocapillary model developed by Higgins and Scriven considered both capillary and viscous forces to govern the operating limit of a slot-die coating process under vacuum pressure [34]. Like the capillary model, this model forces the downstream meniscus to pin at the downstream slot-die corner. However, the upstream meniscus is free to pin along the slot die within the coating gap. The operating limit is given by

$$\frac{6\mu Vl}{h^{2}} - \frac{12\mu Vlt}{h^{3}} + \frac{1.34\text{Ca}^{2/3}\sigma}{t} - \frac{\sigma(\cos\theta + \cos\theta_{s})}{h} \le \Delta P$$

$$\le \frac{12\mu Vl}{h^{2}} - \frac{12\mu Vlt}{h^{3}} + \frac{1.34\text{Ca}^{2/3}\sigma}{t} - \frac{\sigma(\cos\theta + \cos\theta_{s})}{h} \tag{3}$$

where μ is the solution's viscosity, V is the coating speed, and θ_s is the static contact angle of the upstream meniscus against the

slot-die surface. The minimum film thickness can be determined by setting the lower bound of inequality Eq. (3) to zero. Our system does not utilize a vacuum pressure due at the upstream meniscus as having a vacuum box would constrain the layer-by-layer operation and reduce the overall throughput of the process. Therefore, an operational range cannot be accurately determined from these described models. Additionally, both models assume the downstream pinning location to be at the slot-die edge, which limits the operational range of the coating process. From previous studies and experimental results, the downstream meniscus cannot reliably be pinned at the slot-die edge; therefore, we investigate an operational range that allows for a downstream dynamic contact line that can go beyond the slot-die edges [35,36]. Lin et al. found for a large die angle the downstream meniscus likely pins on the outside shoulder [36]. One of the proposed solutions to minimize this effect involved altering the die geometry; however, it is difficult to change die geometry because that would require machining new die for each set of processing conditions. Additionally, the coating windows vary widely based on the type of solution coated and the experimental setup. Therefore, the predicted minimum film thicknesses obtained from these models might not be precisely adapted to our system. Hence, there is a need to develop a model that can determine an operational window for a specific fluid rheology and operational setup of the μ -SLS process.

1.5 Motivation Behind This Work. The following work presents a discussion of the slot-die coating setup for the μ -SLS process and a computational fluid dynamics (CFD) investigation of the limiting process parameters for achieving a desired film thickness for single layer coating. Despite the unique advantages of engendered by the slot-die coating process for nanoparticle bed deposition for μ -SLS applications, the intermittent nature of the process needs a more detailed exploration to understand the coating mechanics. Initial experimental studies on this process have revealed a need to develop computational models to track the free surface flow and meniscus formation process. Previous analytical models that quantify the film thickness as a function of capillary number such as the capillary model and viscocapillary model

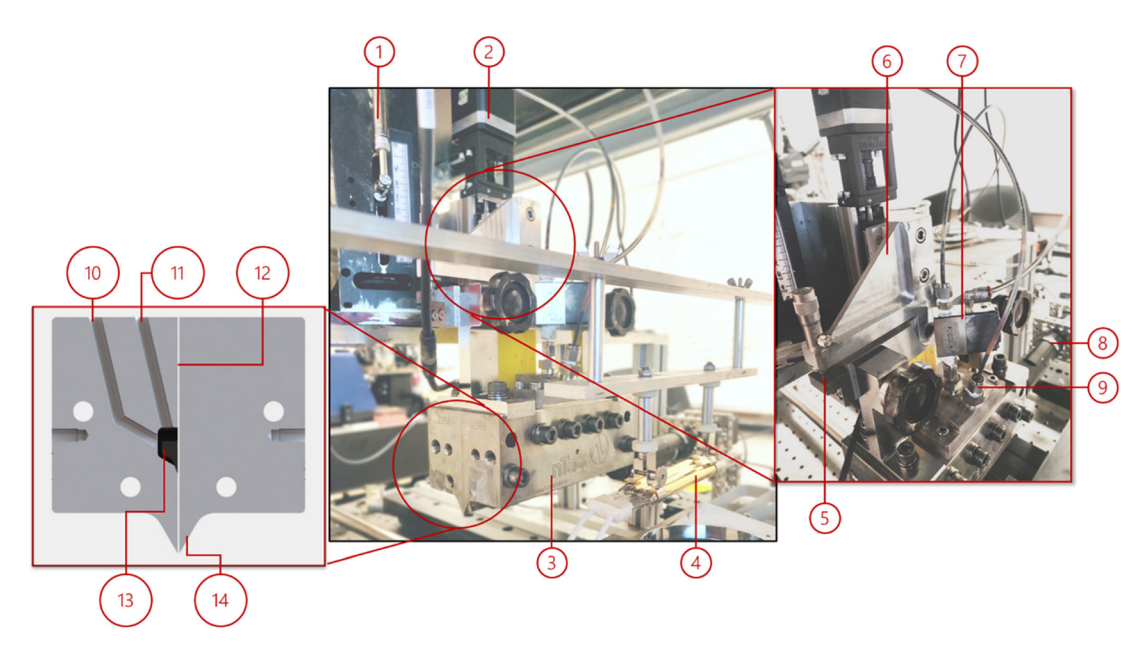


Fig. 2 Design embodiment of the slot-die coating system for μ -SLS. The following components have been shown in the figure: 1. Syringe pump 2. Vertical positioner 3. Slot-die head assembly 4. IR heater 5. Micrometer screw for tip-tilt correction 6. Pivoting bracket 7. Air pilot valve 8. Flow visualization setup 9. Slot-die coater inlet. The left inset figure shows a cross section of the slot-die coater with the following labels: 10. Fluid inlet 11. Air pilot valve connection 12. Die gap 13. Distribution reservoir 14. Die lip.

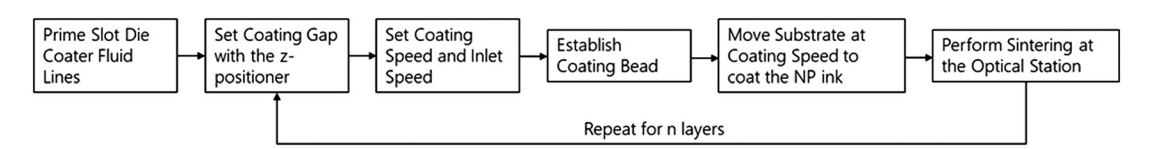


Fig. 3 Schematic representation of the slot-die coating process adapted for nanoparticle bed deposition in the μ -SLS tool

define a set position for the meniscus location, which might not be representative of recorded operational conditions. Additionally, the liquid properties such as surface tension, viscosity, and contact angle vary drastically between different studies, which makes it imperative to develop a simulation framework to determine the operational range. This study presents a CFD model that captures the key parameters of the slot-die coating process and outlines an operating region within which thin sub-5 μ m dry/partially dry film thicknesses can be repeatably obtained. These physics-based two-phase models are required to explain the underlying phenomena and optimal process parameters required for the slot-die coating process.

2 Slot-Die Coating Process Components and Schematic

The experimental setup of the slot-die coater with the different subcomponents is shown in Fig. 2. The slot-die coating system consists of the positioning mechanism, syringe pump, and the die assembly. The positioning mechanism is used to translate the die vertically over the substrate to set the coating gap. It consists of a precision ball screw-based linear rail driven by a 0.36 deg microstepping motor, which can achieve a position repeatability of 3 μ m. A cylindrical flexural pivot is used to enable in-plane positioning of the die head and ensure the parallelism of the lips with the substrate. The syringe pump (Kloehn/IMI Norgren V6 series) consists of a zero dead volume tip syringe with a 60 mm stroke, driven by a brushless DC (BLDC) motor. The syringe pump also includes a three-way rotary valve assembly operated by a NEMA 23 stepper motor to alternate between the intake, aspiration, and distribution functions with the slot-die coater. The coating gap between the die and the substrate is measured using a laser triangulation sensor

(Keyence IL030). The die gap is set using a 50 μ m (2 mil) polyether ether ketone shim. Figure 3 shows a detailed schematic of the steps critical for the startup and continuation of the slot-die coating process in the μ -SLS system. First, the fluid lines connecting the syringe pump to the slot-die coater is primed with the NP ink to ensure no air bubbles inside the system. The die lips are then zeroed on to the substrate to establish the home position and then moved using the vertical positioner to set the coating gap, which is measured by the laser triangulation sensor. The slot-die coater is then primed with the NP ink and purged of the air bubbles to establish the initial coating bead. Next, the substrate is moved underneath the coater to spread the ink across the substrate, while continuously replenishing the slot die with ink. As the substrate starts moving at the specified coating speed, the inlet flow rate of the liquid entering the die is kept constant at a rate that can maintain a stable bead. The upstream meniscus of the bead is under ambient pressure as a vacuum chamber is not used in this study due to the design constraints in an intermittent layer-by-layer coating process. The coated layer then passes under an IR heater (Heraeus Noblelight America LLC, 600 W) to remove excess solvent and partially dry the ink before moving under the optical station for sintering. Previous work [37] on design and preliminary studies with the slot-die coating setup showed that it is expensive to understand the process with just using experimental studies and it needs some baseline understanding of the slot-die coating process physics using simulation models.

3 Development of the Computational Fluid Dynamics Model

The experimental investigation of slot-die coating parameters to identify a nominal operating region is resource and time

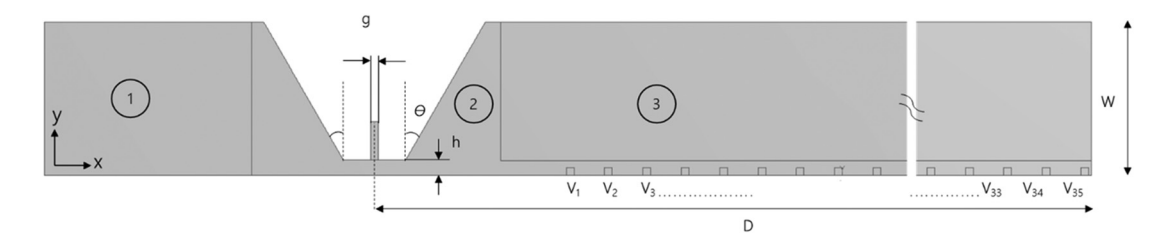


Fig. 4 Representation of the 2D CFD simulation domain divided into the following sections—1. upstream region, 2. menisci region, and 3. downstream region. In this figure, g is the die gap (50 μ m), h is the coating gap (50–150 μ m), θ is the die angle (45 deg), W is the width of the domain (2 mm) and D is the length of the domain (10 mm). Here, the subzones are defined as $V_1, V_2, V_3, \ldots, V_{35}$.

intensive. To further analyze the physics behind the coating process, a 2D, transient Volume-of-Fluid-based CFD model was developed and simulated using ANSYS ACADEMIC FLUENTTM Release 18.1. In this section, we outline the CFD model to understand the meniscus formation, free surface tracking, and effect of key variables on the final wet film thickness of the ink. The CFD model was built using the following design considerations—(1) Identify the key material properties to approximate the ink rheology, (2) Define the geometric domain, (3) Setup the meshing parameters to accurately capture the effects of the free surface flow, (4) Specify the boundary conditions to emulate experimental settings, and (5) Select the numerical solvers to solve a system of coupled, linearized algebraic solutions.

In the slot-die coating process, the air in the geometric domain is displaced by the coating ink, which results in a two-phase flow field. One of the most robust modeling frameworks for two-phase flow investigation is the volume-of-fluid (VOF) method, which is used to track the interfaces between the fluids. The VOF method calculates the scalar volume fraction of the liquid, α_{ink} , which is the volume occupied by the discretized computational cell. The value of α_{ink} is zero when the cell does not contain any liquid and is set at one when it just contains the liquid. At the interface, the value of varies α_{ink} from zero to one to indicate the presence of both fluids. The model for the volume fraction is given by Eq. (4)

$$\frac{\partial \alpha_{\text{ink}}}{\partial t} + \boldsymbol{u} \cdot \nabla \alpha_{\text{ink}} = 0 \tag{4}$$

where \mathbf{u} is the velocity vector components in x and y-directions and α_{ink} is volume fraction of the ink at a given time-step. The VOF framework in FLUENT can be used to solve for coupled multiphase flow of two or more immiscible fluids by solving for a single set of velocity and momentum equations and tracking the volume fractions of the fluids throughout the computational domain. The method can be used with a pressure-based solver and must have regions within the domain predefined with the fluid, which depends on the nature of the problem.

3.1 Geometric Domain and Meshing. The computational domain used in the study is illustrated in Fig. 4. The domain was modeled based on the actual geometry and experimental design of the slot-die coater to include a 50 µm die gap, a coating gap varying from $50-150 \,\mu\mathrm{m}$ and die land angles of 45 deg. The domain is divided into the following sections to enable differential meshing and reduce the computational load—(1) upstream region, (2) menisci zone, and (3) downstream region. The menisci zone represents the overall area within which the meniscus is supposed to exist and has been divided into 35 equally spaced subzones of $50 \,\mu\text{m} \times 50 \,\mu\text{m}$ to extract the volume fraction of the liquid and track the film thickness at different time-steps along the length of the domain. The entire plane is meshed using a combination of smooth quadrilateral elements and refined to have a 2.5 um element size in the menisci zone to ensure a good interface tracking and the 10 μ m everywhere else. Initially, a smaller computational

domain was defined to ease the computational load, but a longer downstream domain was defined to capture the uniformity in film thickness.

3.2 Governing Equations and Boundary Conditions. The temperatures throughout the computational domain are maintained at a constant, which reliably approximates the experimental conditions. Therefore, the energy equation is not solved in this model. For incompressible fluids under flow with negligible inertia, the velocity vector field can be solved using the continuity and momentum equations along the x- and y-directions and shared between the different phases, which are given by

$$\frac{\partial \rho}{\partial t} + \nabla \cdot (\rho \mathbf{u}) = 0 \tag{5}$$

$$\frac{\partial(\rho \mathbf{u})}{\partial t} + \nabla \cdot (\rho \mathbf{u} \mathbf{u}) = -\nabla P + \nabla \tau + \rho g + F_{\text{st}}$$
 (6)

where ρ is the density, \mathbf{u} is the velocity vector components in x and y-directions, P is the pressure, τ is the stress tensor, g is the acceleration due to gravity, and $F_{\rm st}$ is the source term to capture surface tension effects. These intermolecular forces at the interfaces of the fluids are modeled using the continuum surface force framework developed by Brackbill et al., treating it as a 2D effect across the interface [38]. For two-phase flow, the source term incorporated in the momentum equation due to surface tension effects is given by

$$F_{\rm st} = \sigma \frac{\varepsilon \nabla \alpha_{\rm ink} (\alpha_{\rm ink} \rho_{\rm ink} + \alpha_{\rm air} \rho_{\rm air})}{0.5 (\alpha_{\rm ink} + \alpha_{\rm air})} \tag{7}$$

where σ is the surface tension and ϵ is the curvature of the interface.

The boundary conditions are set to emulate the experimental setup of the slot-die coating process. Figure 5 shows the different boundary conditions used in the study. The domain is at a constant atmospheric pressure of 101 kPa. The effects of gravity are considered at a negative y-direction 9.81 m/s². The inlet is taken as a velocity inlet for the desired liquid that can be defined for any flow rate. The inlet area in between the slot-die lips is predefined with a volume fraction of 1 (100% liquid) prior to the start of the simulation to emulate a slot die filled with liquid. The slot- die walls, which include the inlet as well as the exterior walls, are taken as no-slip stationary walls with a standard roughness model of roughness constant 0.5. The slot-die surfaces have a constant contact angle with the liquid as described by goniometer measurements of the NP ink. Wall adhesion is considered to account for the contact angle curvature of the surface near the wall. The substrate is a moving wall toward the positive x-direction set at the desired wetting speed. The substrate, similarly, has a no-slip condition and uses the standard roughness model. The subzones defined are taken as an interior zone where no interaction occurs

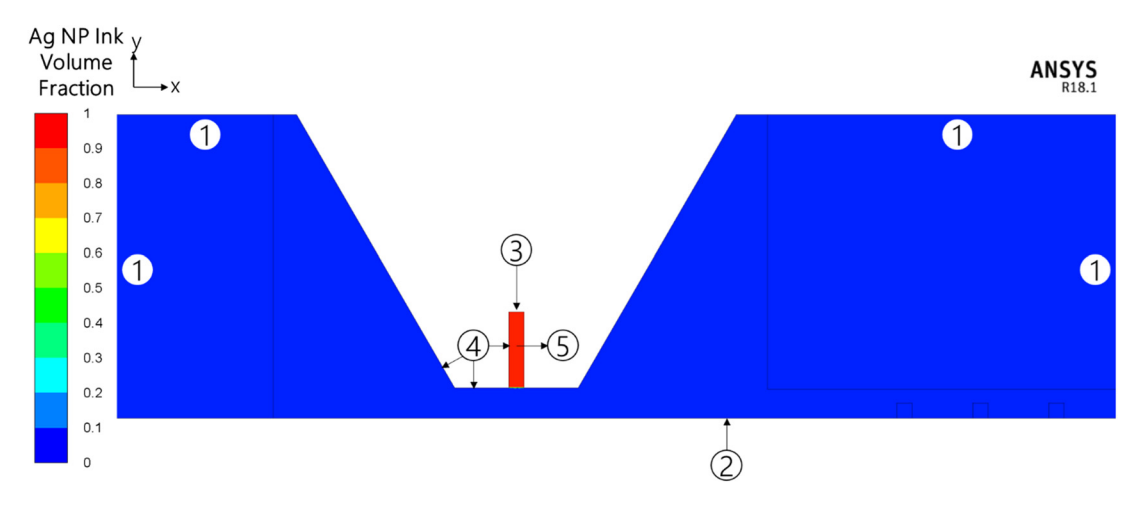


Fig. 5 Representation of the boundary conditions (BCs) setup in the CFD model. 1. Atmospheric pressure condition ($P_{\rm gage} = 0$), 2. Moving wall condition specified by the coating speed in mm/s 3. Fluid inlet BC 4. Noslip stationary wall condition 5. Patched zone to predefine a region with Ag NP ink.

between the interfaces. An atmospheric pressure outlet is set as the surrounding boundary of the slot-die domain.

3.3 Numerical Methods. The VOF framework defined within FLUENT, Release 18.1 provides an option for explicit and implicit formulation based on the problem definition. The explicit formulation has been explored by coating models to accurately track and differentiate between the interfaces [39,40]. However, it is applicable for transient models only and the time-step is limited by the Courant number, which can introduce divergence errors during the solution. The most used interface tracking scheme is Geo-reconstruct, which has a high accuracy if a sharp interface is desired, but the convergence speeds are slower. Conversely, the implicit model is suitable for both steady-state and transient calculations, does not have a Courant number limitation and can be run with larger time steps. This is critical for the length scales at which the current slot-die coating simulation is being run where the domain length is approximately two orders of magnitude larger than the slot-die gap and the coating gap in order to accurately determine the film thickness after achieving a good coating bead stability. The compressive scheme within the implicit VOF framework provides an optimal combination of accuracy and speed compared to the first order, second order, QUICK and modified HRIC scheme [41,42]. However, the numerical diffusion at the interface does not accurately capture its curvature and present a sharp boundary between the two phases, which might be a source of error for the simulation results. To counter that, the film thickness is averaged across the last five subzones to obtain a film thickness window. The pressure and velocity are coupled using the SIMPLE scheme and discretized throughout the domain using the PRESTO and second-order upwind, respectively. The underrelaxation factors of 0.3, 1, 1, and 0.7 are used for the pressure, density, body forces and momentum, respectively.

4 Results and Discussions

4.1 Experimental Procedure. Commercially available silver nanoparticle inks (Novacentrix Metalon Conductive Ink, JS-A102, Austin, TX) designed to produce highly conductive electrical circuits for printed electronics applications was used as part of the experimental study. The key physical properties of the ink based on the manufacturer's specifications are outlined in Table 2. These properties were also used in the setup of the simulation model to accurately define the fluid. Inlet flow out of the slot-die coater for varying syringe speeds was approximated using mass conservation law, lengths of the pipes, and slot-die coater reservoir and gap volume. It was measured by collecting the volume of

fluid output from the die exit for the time that takes the syringe to provide $60\,\mathrm{mL}$ of fluid to the slot-die coater (also known as the syringe speed). The need for measurement was to get a rough estimate of the range of inlet speeds that must be defined for the simulation to be representative of the actual process. An in situ flow visualization setup was developed using a CMOS camera (Sentech/Omron STC-HD133DV) to track the meniscus formation and spreading across the substrate (Fig. 6(a)).

The experiment consists of varying the coating speed and flow rate. A constant coating gap of 100 μ m is used for each trial. The experimental syringe speed was set such that enough fluid is provided into the slot-die system to maintain a stable coating bead throughout the coating process. The 60 mL syringe limited the maximum syringe speed that can be achieved before all the liquid was dispensed. The silver NP ink was coated onto $50 \,\mathrm{mm} \times 75 \,\mathrm{mm}$ glass slides. The experimental parameters revolved around the physical limitations of the slot-die coating system, given by the syringe volume and substrate size. The resultant film deposited onto the substrate was visually validated, with the help of the CMOS camera, to be free of defects such as coating bead breakup, neck-in, air entrainment, and streaks. Figures 6(a) and 6(b) shows the flow visualization setup and the coating process as captured by the camera. The coating gap domain is quickly overflowed with liquid at the start of the coating process but as the glass substrate is dragged along the x-direction the upstream and downstream meniscus quickly forms and reaches a steady-state (i.e., the pinning location does not vary significantly, thereby maintaining a uniform coating thickness) at about 2.4 s into the coating process. The in situ flow visualization allowed for adjustments in the experimental parameters as needed. The verification ensured that an optimal operating range were used to deposit repeatable film thicknesses. After verification of film quality, the coated substrate is placed on top of a 100 °C hot plate to remove the NP ink solvent. The dry film thickness was then recorded using an optical profilometer (Keyence VK-X1100) at nine different locations. Due to the initial startup of the coating process, high and nonuniform thicknesses were seen at regions

Table 2 Silver nanoparticle ink specifications

	Novacentrix JS-A102	Units
Ag content	40	Wt%
Viscosity	8–12	cP
Surface tension	19–30	dyne/cm
Z-avg particle size	30-50	nm
Specific gravity	1.6	Dimensionless

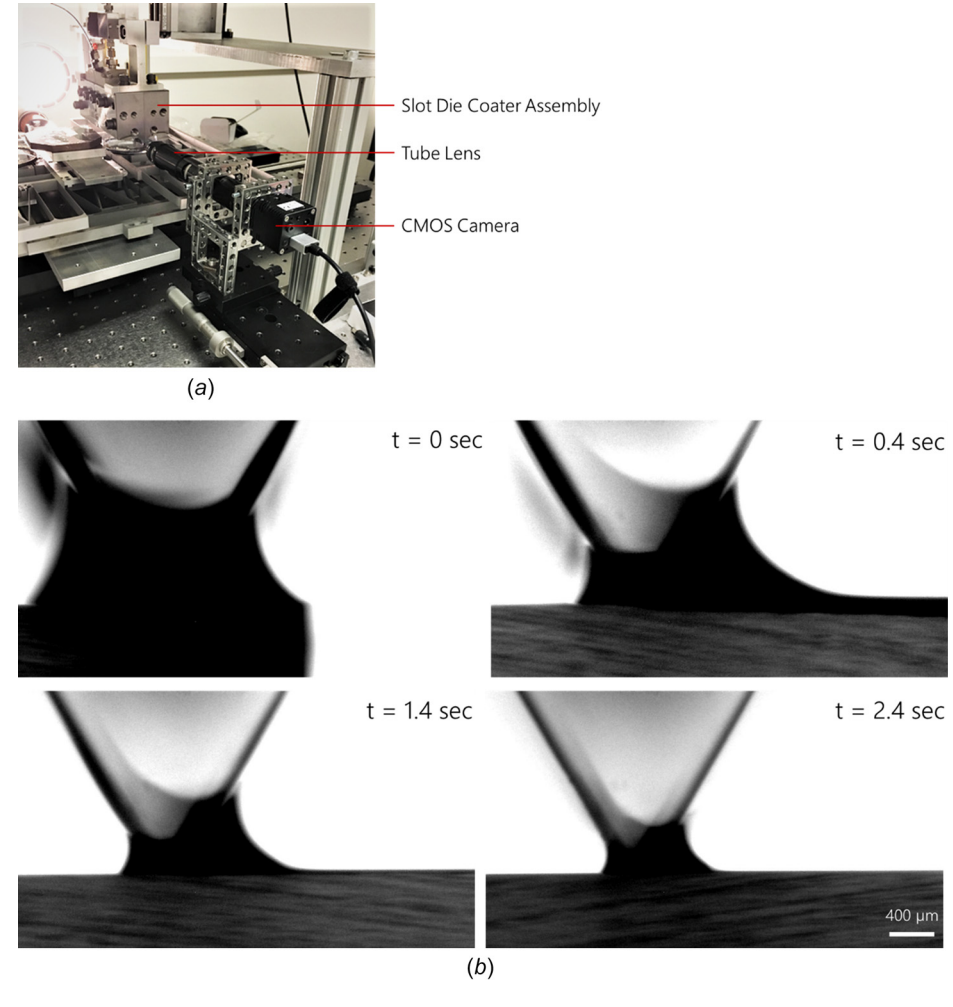


Fig. 6 (a) Flow visualization camera setup focused on the slot-die coating exit. (b) Camera images to track the establishment and progression of the coating bead for the coating speed of 10 mm/s and a coating gap of 100 μ m through times t=0-2.4 s At around 2.4 s, the upstream and downstream meniscus pinning location undergoes minimal variation, thereby indicating better coating uniformity.

where the coating bead has not yet stabilized. Therefore, only the region along the sample where the coating bead stabilized were considered. The dry film thickness was then converted to wet film thickness using the weight percent loading of silver to solvent.

4.2 Computational Fluid Dynamics Results Discussion.

The 2D time-dependent CFD model forwarded in this study was used to obtain the resulting film thicknesses and the uncertainties associated with them for a range of parameters. A three-factorial design of experiments, as outlined in Table 3, was developed to obtain single layer thicknesses. The three main parameters simulated in this study are—inlet speed (mm/s), coating speed (mm/s) and coating gap (μ m). As mentioned in Sec. 3, the die gap was fixed at 50 μ m and the computational domain was extended to capture the film thickness uniformity. The film thickness was determined by spatially averaging the volume fraction encompassed by the last five subzones defined within the computational domain and multiplying it by the area of the subzone. The following sections (Secs. 4.2.1–4.2.3) provide the trends obtained from the simulation results.

4.2.1 Effect of Inlet Speed (mm/s) on the Coating Bead Stability and Film Thickness Uniformity. Using the CFD model, the meniscus formation and resulting film thickness can be visualized. The variation of the coating bead location and size with the inlet speed has been shown in Fig. 7. While there was no clear trend

Table 3 CFD Simulation design of experiment parameters and setup

Parameter	Value	Units
Inlet speed	2.5, 5, 7.5, 10, 12.5, 15, 17.5, 20, 22.5, 25	mm/s
Coating speed	2.5, 5, 7.5, 10, 12.5, 15, 17.5, 20, 22.5, 25	mm/s
Coating gap	50, 100, 150	μm
die gap	50	μm
Ink	Novacentrix Metalon JS-A102 Ag NP ink	•
Ink viscosity	10	cP
Ink surface tension	25	dyn/cm
Ink specific gravity	1.6	-
Ink contact angle	0.5	degrees

seen on the wet film thickness for varying inlet speeds, tracking the coating bead position for varying inlet speeds within the domain provided critical information about the bounds of the coating region and the onset of defects. The lower bound of the simulation results in an unstable coating bead as shown in Fig. 7 top left, where the upstream meniscus recedes back toward the slot-die exit. This can cause bead breakup resulting in regions without any coated liquid on the substrate. As the inlet velocity is gradually increased to 5 mm/s, the coating bead stabilizes and has meniscus pinned near the slot-die shoulders. As it can be seen in Fig. 7 top right, this behavior is similar to the downstream

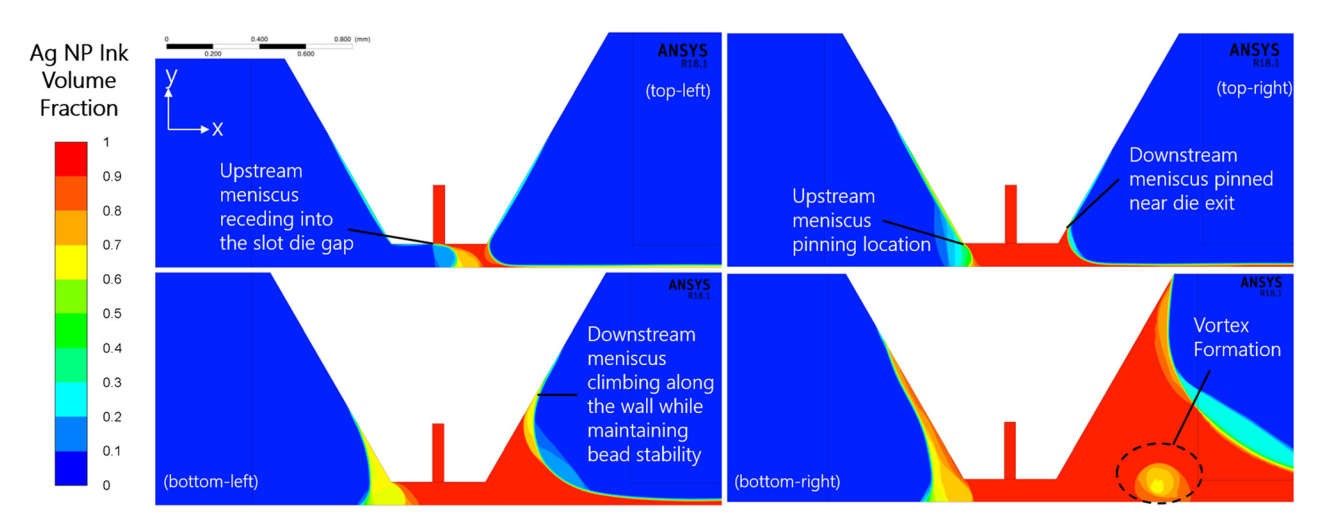


Fig. 7 VOF contour plots to visualize coating bead stability for varying inlet speeds. The bead stability and onset of defects for coating speed of 25 mm/s and the following inlet speeds have been shown (top left)—2.5 mm/s (top right) 5 mm/s (bottom left) 10 mm/s (bottom right) 25 mm/s. As it can be seen from Fig. 7 top left, the coating bead starts to recede into the slot-die exit, thereby indicating a bad coating due to eventual bead break up. The beads remain stable in top right and bottom left figures. However, as seen in bottom right figure, higher inlet speeds lead to formation of vortices and air bubbles within the menisci zone, leading to air entrainment defects.

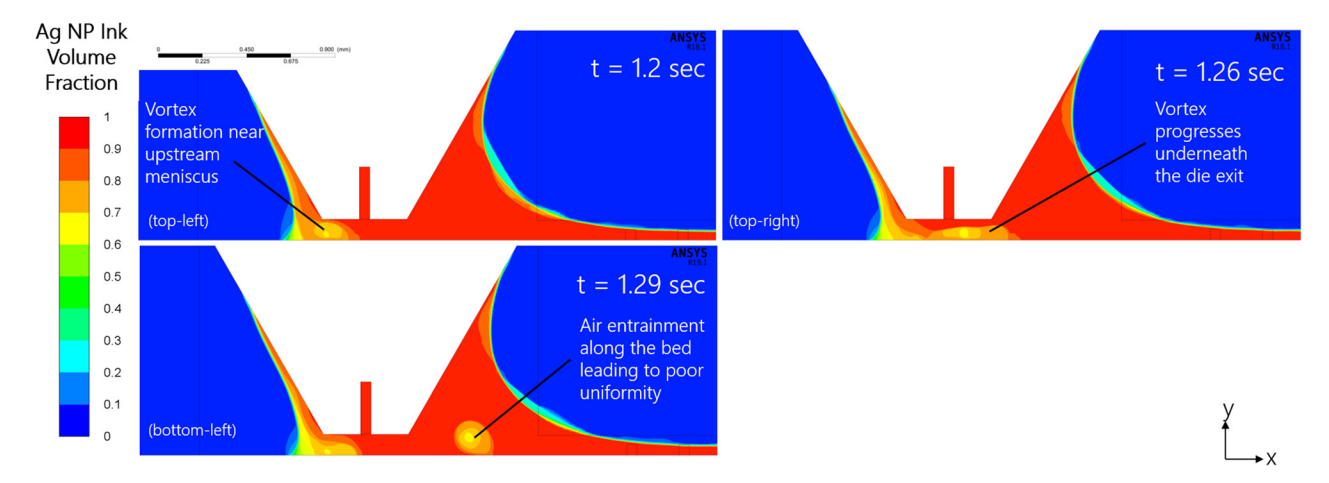


Fig. 8 Tracking vortex formation leading to air entrainment defects for a coating gap of $100 \,\mu\text{m}$, inlet speed of $20 \,\text{mm/s}$ and coating speed of $25 \,\text{mm/s}$ through visualizing the bubble formation in the VOF contour plots. (top left) At this time-step, the vortex starts forming near upstream meniscus, indicating potential air entrainment (top right). The vortex spreads across the bed as the ink is coated (bottom left) $t = 1.29 \,\text{s}$.

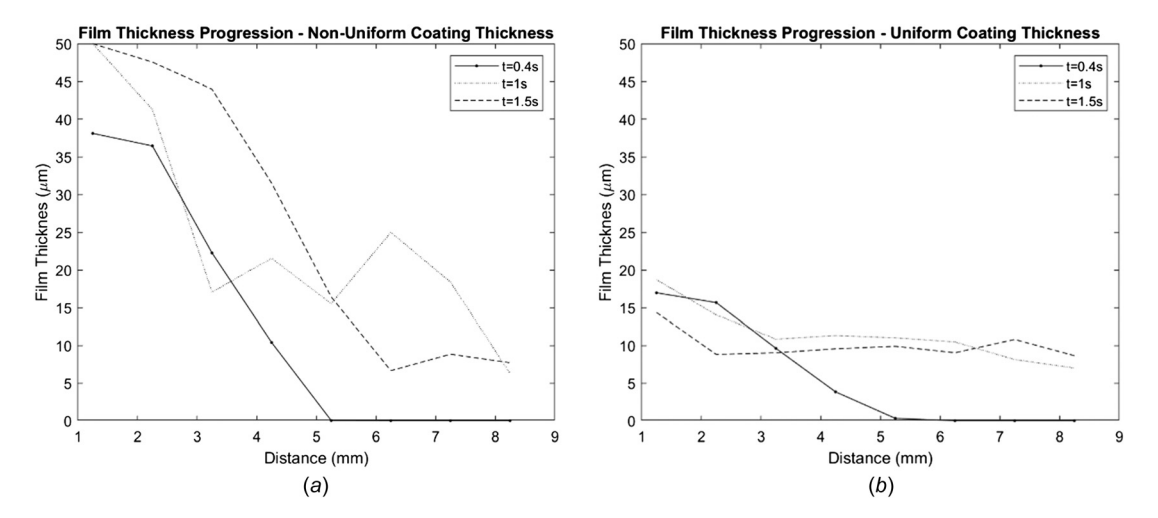


Fig. 9 Tracking Ag NP ink film thickness progression across the subzones within the domain at different time-steps. (a) Example of a uniform thickness output (coating gap = $150 \,\mu\text{m}$, inlet speed = $7.5 \,\text{mm/s}$, coating speed = $20 \,\text{mm/s}$). (b) Example of a nonuniform thickness output (coating gap = $100 \,\mu\text{m}$, inlet speed = $25 \,\text{mm/s}$, coating speed = $15 \,\text{mm/s}$).

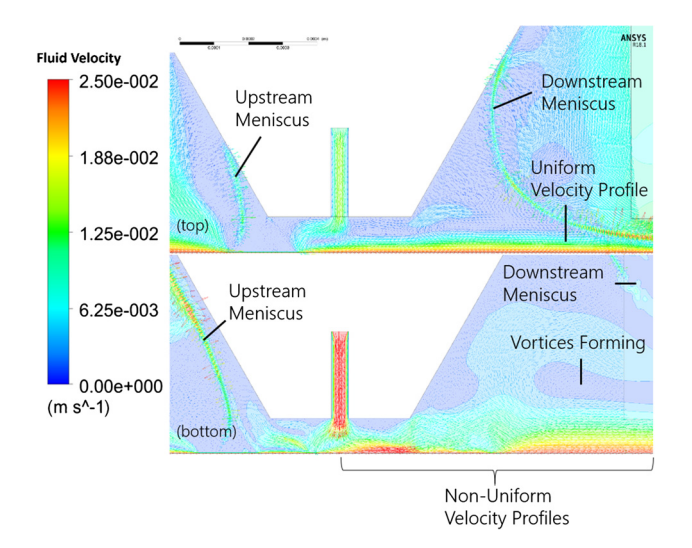


Fig. 10 Fluid velocity contours tracking the coating bead stability for coating gap at $100 \, \mu m$, coating speed 25 mm/s and inlet speed (top) 10 mm/s (bottom) 25 mm/s

meniscus pinning entailed in previous studies. The coating bead maintains its stability at higher flow rates such as 10 mm/s as the downstream climbs up along the lower slot-die shoulder, as shown in Fig. 7 bottom left. The stability of the bead is also related to the position of the upstream meniscus. As it climbs too high, with an increase in the inlet speed, as shown in Fig. 7 bottom right, the

coating defects start to appear such as air entrainment and large vortices in the downstream meniscus region, which marks the upper bound of the coating window.

The development of defects such as air entrainment is captured within the VOF contour plots where the coating parameters fall outside the operational range because of an unstable bead. Figure 8 shows the development of a bubble as air is trapped inside of the coating gap. The air entrainment causes nonuniformities within the resultant film thickness, forming ripples that cause the film thickness to be thicker at random positions along the length of the substrate.

The nonuniformity in deposited film thicknesses is further captured by plotting the film thickness for subzones along the domain versus the simulation time. Figure 9(a) shows the film thickness development for a stable coating bead where the initial peak in film thickness around 0.6 s is the region where the coating bead is first stabilizing. The film thickness for each subzone across the domain then stabilizes around a constant film thickness, this is categorized as a stable coating bead that has reached a steadystate. This initial high film thickness during the startup of the coating process shows a trend similar to the variation in the experimental film thickness measurements along the coated sample. Design points where the flow rate is higher than the coating speed results in coating bead instability. This leads to uneven downstream meniscus growth and formation of large vortices. The unstable coating bead and vortices cause ripples where excess liquid is coated onto the substrate deteriorating the uniformity of the deposited thin film. Figure 9(b), shows the ripple effect in action where the film thickness remains unstable after the initial formation of the coating bead. A second peak in film thickness at 1.3 s indicates excess liquid deposition onto the substrate.

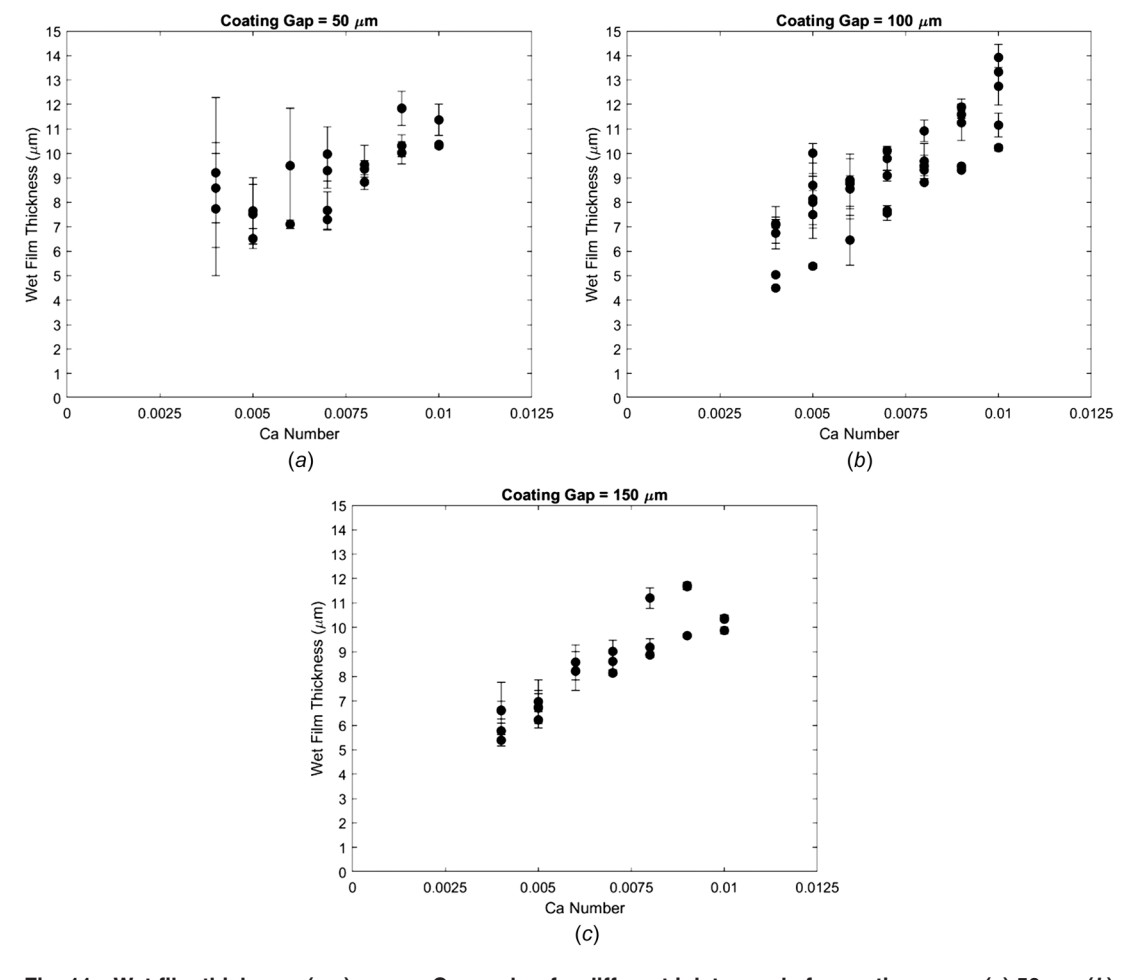


Fig. 11 Wet film thickness (μ m) versus Ca number for different inlet speeds for coating gaps: (a) 50 μ m, (b) 100 μ m, and (c) 150 μ m. The operating points shown in these curves correspond to the film thicknesses within the desired range. The plots show different inlet speeds for the same coating speed and gap.

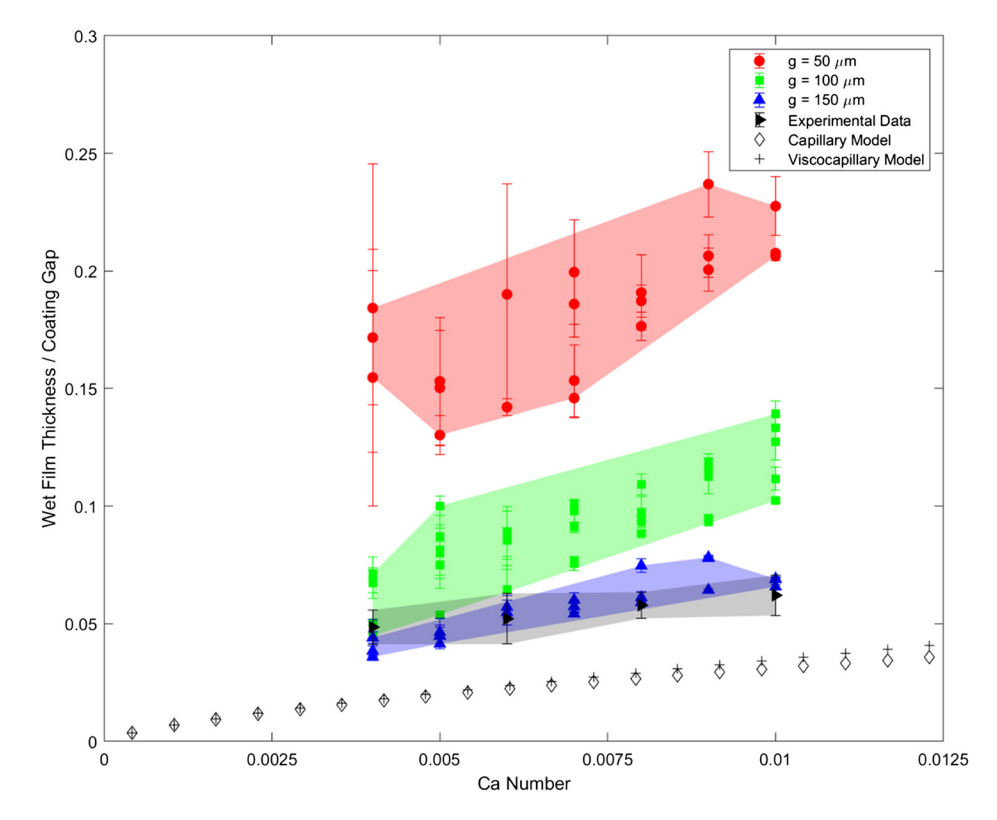


Fig. 12 Plot of wet film thickness (t) normalized by the coating gap (g) versus the Ca number for varying coating gaps and experimental coating for an inlet speed of 10 mm/s and coating gap of 100 μ m. The t/g ratio increases with the substrate speed and coating gap, following a similar trend outlined by theoretical models present in the literature.

The instability in the coating bead can also be visualized in the velocity contours plots shown in Fig. 10. For a given flow rate and coating speed that yield uniform coating, the velocity contour shows a steady coating bead that has minimal to no vortices formation in either the upstream or downstream meniscus. Meanwhile, for a flow rate that exceeds the coating speed, the bead is unstable and large vortices form in the downstream meniscus that result in air entrainment and irregular film deposition. Physically, it shows that the inlet speed of the fluid is unable to provide enough fluid for the speed at which the coating happens, thereby leading to regions of uneven coating thickness, which manifest in the form of nonuniform coating and zones without any liquid in the actual experiments. Therefore, for a flow rate that exceeds the coating speed, the downstream meniscus tends to grow large enough to cause excessive vortices to form in the meniscus that result in defects. From these recorded defects, an operational window can be determined for uniform film thickness.

4.2.2 Investigation of Coating Speed (mm/s) versus Film Thickness (µm) for Varying Coating Gaps (µm). Using the CFD model and the outlined design of experiments, several simulations were carried out to understand the effect of coating speed on the wet film thickness. Based on the simulation results, the set of design parameters for which the wet film thicknesses were above 15 μ m and where coating defects were seen are filtered out as they are outside the desired range for our applications. See Supplemental S2 available in the Supplemental Materials on the ASME Digital Collection provide plots for each design parameter simulated which show the points outside the operating range. These points were filtered out of the data shown in Figs. 11 and 12 because they were either leading to nonuniform and high coating thicknesses or causing air entrainment and other associated defects. Figure 11 shows the variation of wet film thickness as a function of capillary number for different coating gaps. As the capillary number increases, the wet film thickness increases if there is sufficient fluid to maintain a coating bead. The increase in film thickness is consistent for each coating gap, $50\,\mu\text{m}$, $100\,\mu\text{m}$, and $150\,\mu\text{m}$. The wet film thickness versus Ca number follows the same trend as found in the experimental results. From the perspective of the $\mu\text{-SLS}$ process, Fig. 11 shows the set of operating points, which can attain wet film thicknesses from 4 to $14\,\mu\text{m}$. These results can be used to identify the operating range to obtain a certain thickness based on the required resolution of the microscale part being formed.

4.2.3 Investigation of Coating Gap (µm) versus Film Thickness (µm) for Varying Coating Speeds (mm/s). The wet film thickness (t) is normalized by the coating gap (h) to obtain a comparable metric, to obtain a dimensionless t/h ratio. The CFD results have a trend similar to the theoretical capillary and viscocapillary models. Figure 12 outlines the variation of the t/g ratio for different Ca numbers and outlines the regions within which a uniform coating can be achieved. The previous models and our results follow the same trend of increasing film thickness as the capillary number increases. The t/h ratio increases with the Ca number and each coating gap has a different range within which a uniform film thickness is achieved. The difference in t/h ratio for a 100 μ m coating gap between the CFD results and theoretical models may result from simplifications that derive from Couette and Poiseuille flow using which the theoretical models are developed. Furthermore, the difference between the experimental data for 10 mm/s inlet speed and 100 μ m coating gap can be explained by the nonlinearities in the experimental setup, while setting up the coating gap and the vibrations produced by the translation system. The CFD results indicate that such analytical equations for predicting film thickness may fall short when fluid-gas interface, contact lines, and other fluid rheological effects are considered. It is important to characterize this operating region to identify the limits to the process throughput, while satisfying the requirement to have a uniform coating zone. It must be noted that as outlined in the previous

Table 4 Regression model parameters and statistics

Coefficient	Estimate	<i>p</i> -value
Intercept (β_0) Inlet speed (β_1) Coating speed (β_2) Coating gap (β_3)	$\begin{array}{c} 4.639 \\ -4.939 \times 10^{-5} \\ 3.119 \times 10^{-4} \\ -6.525 \times 10^{-3} \end{array}$	$3.16 \times 10^{-10} \\ 0.182 \\ 3.228 \times 10^{-19} \\ 0.0507$

Model: wet film thickness = $\beta_0 + \beta_1$ (inlet speed) + β_2 (coating speed) + β_3 (coating gap) + (error)

sections (Secs. 4.2.1 and 4.2.2), the points outside the regions presented in Fig. 12 present an unstable coating bead and uneven meniscus, leading to poor coating uniformity and very high coating thicknesses. These trends also define the operating points for multiple layer coating. However, the coating window is hypothesized to be smaller for layer-by-layer coating depending on the interlayer interaction between layers with varying liquid viscosities, as the previously coated layer undergo partial drying and sintering.

4.2.4 Model Fitting. The simulated model was further evaluated using a multivariate linear regression model to understand the dependence of the coating thickness on the three main process variables—coating speed, inlet speed, and coating gap. The model details and statistics are presented in Table 4. The refined simulation data consisted of 86 design points within the desired film thickness range. The data were randomly partitioned to create training (85%) and cross-validation (15%) sets. The objective behind this was to avoid overfitting of the data while using more advanced regression models, like artificial neural networks (ANNs) or support vector machines (SVMs). However, the performance of these machine learning models was comparable to that of the multivariate linear regression model. The details of the model formulation and predicted thickness values using various models are presented in the Supplementary Information available in the Supplemental Materials on the ASME Digital Collection. Figure 13(a) shows the departure of the residuals from following a normal distribution, characterized by the heavy tails. The model was used to predict the film thickness of the validation dataset, which yielded a mean absolute error of 9.2% between the predicted value and simulated value across the validation dataset. The model predicted thickness for the experimental parameters shown in Fig. 12 had a mean absolute error of around 27.5%. Figure 13(b) shows the model predicted thicknesses against the simulated thicknesses. As seen in Table 4, the changes in the inlet speed predictor are not significantly affecting the wet film thickness, which affirms the simulation results discussions presented in the previous sections (Secs. 4.2.1–4.2.3) that the inlet speed must

be sufficiently high to avoid coating bead breakup. Therefore, according to the model, the wet film thickness can be changed by changing the coating speed and coating gap, if a sufficient inlet speed is maintained to avoid coating defects. According to the model, for the same coating gap and inlet speed, to obtain a wet film thickness increase of $1\,\mu\text{m}$, the coating speed must be changed by $3.2\,\text{mm/s}$.

5 Conclusion

A slot-die coating approach for film forming to lay down metallic nanoparticle beds in a microscale additive manufacturing system has been outlined in this paper. In addition to an experimental validation of the technique for single layer coating, a CFD model is created that can determine an operating window for a range of parameters. The layer-by-layer slot-die coating process is intermittent in nature, operating without the forced pinning of the upstream and downstream menisci using external vacuum. The model explores a large range of operating parameters as it does not assume downstream meniscus pinning location to be at the slot-die edge. The model parameters were chosen based on the preliminary results where the stability of the coating bead was poor, and there were experimentally verified based on the flowvisualization setup as well. For example, the lower limit of the inlet speed was at 2.5 mm/s based on the models result, where the coating bead started receding back into the slot-die coating exit (as seen in Fig. 7 top left), and the upper limit was set at 25 mm/s, where the coating bead climbs up too high along the shoulder of the slot die and vortices start to form (as seen in Fig. 7 bottom right). The deposited film maintains uniformity as the downstream meniscus pins outside of the slot-die edge until the flow rate nears or exceeds the coating speed. The CFD model expands upon existing models to fit an operational window to our specific experimental setup and fluid properties, which are outside of what can easily be modeled analytically. The results are in good agreement with minimum film thickness predictions with the models presented in the literature. The operating limits are bound by a flow rate such that sufficient fluid must be provided into the slot die to maintain a coating bead and not too high of a flow rate such that the downstream meniscus grows sufficiently to cause large vortices to form. An operational window for each set of coating gaps, $50 \mu m$, 100 μ m, and 150 μ m, is more suitable as the t/h ratio varies for different coating gaps. The model is valid for low capillary number flows (0.003-0.01), which are defined by the fluid properties and the process conditions that are a part of our design space. This model informs the future work based on the knowledge gained from the good operability window for single layer coating and extending it to multilayer coating process.

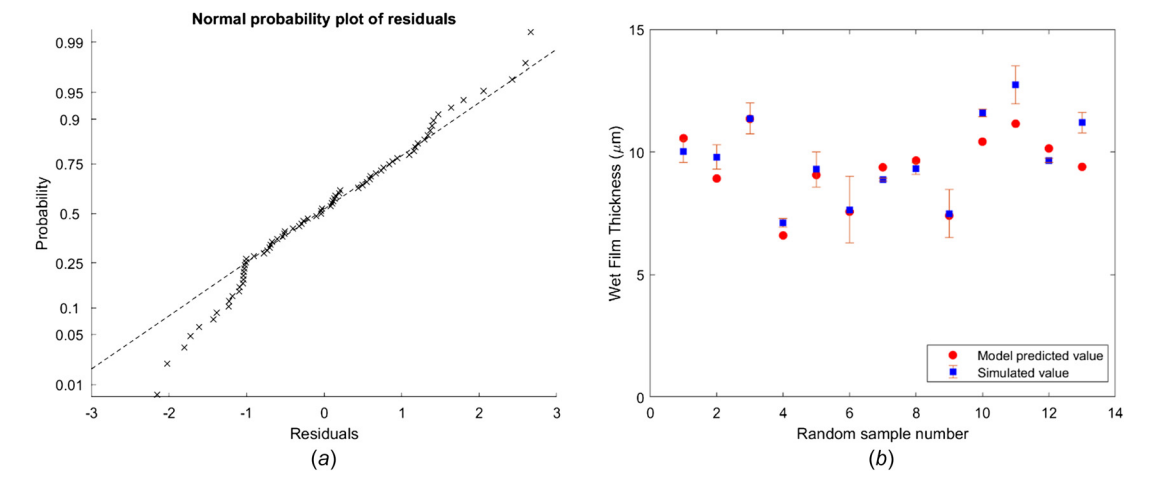


Fig. 13 (a) Normal probability plot of residuals for the training dataset. (b) Predicted wet film thickness versus simulated wet film thickness for validation dataset.

The experimental work done shows the validity of slot-die coating process to reliably deposit sub-5 μ m partially dry films for the μ-SLS additive manufacturing process. The CFD model can extrapolate a coating window for given parameters that yield uniform film thickness free of defects. The simulation and experimental investigation of the coating window will allow for greater control in deposited film thickness for a targeted desired resolution. These single-layer simulation studies will also form the basis of the multiple layer studies where interlayer properties and layeron-layer interactions become significant.

Acknowledgment

This work was made possible by the parallel computing resources at Texas Advanced Computing Center (TACC) and the metrology resources at Texas Materials Institute (TMI). The authors would also like to thank NXP Semiconductors and National Science Foundation for the financial supports provided to this work.

Funding Data

• National Science Foundation (Grant No. 1728313; Funder ID: 10.13039/100000001).

Nomenclature

 $F_{\rm st} = {\rm surface \ tension \ force \ component}$

g = acceleration due to gravity

h =coating gap

t = film thickness

V =coating speed

 α = volume fraction

 ΔP = vacuum pressure between the upstream and downstream meniscus

 $\theta = {\rm contact} \ {\rm angle}$

 $\mu = \text{viscosity}$

 $\rho = density$

 σ = liquid surface tension

 $\tau = stress tensor$

References

- [1] ASTM International, 2013, "Standard Terminology for Additive Manufacturing Technologies," Rapid Manufacturing Association, ASTM International, West Conshohocken, PA, Standard No. F2792-12a.
- [2] Gibson, I., Rosen, D., and Stucker, B., 2015, "Introduction and Basic Principles," Additive Manufacturing Technologies: 3D Printing, Rapid Prototyping, and Direct Digital Manufacturing, Springer, New York, pp. 1–18. [3] Guo, N., and Leu, M. C., 2013, "Additive Manufacturing: Technology, Appli-
- cations and Research Needs," Front. Mech. Eng., 8(3), pp. 215–243.
 [4] Delgado Camacho, D., Clayton, P., O'Brien, W. J., Seepersad, C., Juenger, M.,
- Ferron, R., and Salamone, S., 2018, "Applications of Additive Manufacturing in the Construction Industry—A Forward-Looking Review," Autom. Constr., 89, pp. 110-119.
- [5] Wong, K. V., and Hernandez, A., 2012, "A Review of Additive Manufacturing," ISRN Mech. Eng., 2012, pp. 1–10.
 [6] Zadpoor, A. A., and Malda, J., 2017, "Additive Manufacturing of Biomaterials,
- Tissues, and Organs," Ann. Biomed. Eng., 45(1), pp. 1–11.
- [7] Roy, N. K., Behera, D., Dibua, O., Foong, C., and Cullinan, M. A., 2019, "A Novel Microscale Selective Laser Sintering (μ -SLS) Process for the Fabrication of Microelectronic Parts," Nat. Microsyst. Nanoeng., 5, p. 64.
- [8] Yuksel, A., Yu, E. T., Murthy, J., and Cullinan, M., 2017, "Effect of Substrate and Nanoparticle Spacing on Plasmonic Enhancement in Three-Dimensional Nanoparticle Structures," ASME J. Micro Nano-Manuf., 5(4),
- [9] Yuksel, A., and Cullinan, M., 2016, "Modeling of Nanoparticle Agglomeration and Powder Bed Formation in Microscale Selective Laser Sintering Systems, Addit. Manuf., 12, pp. 204–215.
- [10] Dibua, O. G., Yuksel, A., Roy, N. K., Foong, C. S., and Cullinan, M., 2019, 'Nanoparticle Sintering Model: Simulation and Calibration Against Experimental Data," ASME J. Micro Nano-Manuf., 6(4), p. 041004.
- [11] Lifton, V. A., Lifton, G., and Simon, S., 2014, "Options for Additive Rapid Prototyping Methods (3D Printing) in MEMS Technology," Rapid Prototyp. J., 20(5), pp. 403-412.
- [12] Roy, N. K., Behera, D., Dibua, O. G., Foong, C. S., and Cullinan, M., 2019, "Experimental Study of the Subsystems in a Microscale Additive Manufacturing Process," JOM, 71(3), pp. 974-983.

- [13] Roy, N. K., Behera, D., Dibua, O. G., Foong, C. S., and Cullinan, M. A., 2018, 'Single Shot, Large Area Metal Sintering With Micrometer Level Resolution,' Opt. Exp., 26(20), p. 25534.
- [14] Olakanmi, E. O., Cochrane, R. F., and Dalgarno, K. W., 2015, "Progress in Materials Science a Review on Selective Laser Sintering/Melting (SLS/SLM) of Aluminium Alloy Powders: Processing, Microstructure, and Properties," J. Prog. Mater. Sci., 74, pp. 401–477.
- [15] Bai, Y., and Williams, C. B., 2015, "An Exploration of Binder Jetting of Copper," Rapid Prototyp. J., 21(2), pp. 177–185.
- [16] Keicher, D. M., Smugeresky, J. E., Romero, J. A., and Michelle, L., 2020, "Using the Laser Engineered Net Shaping (LENS) Process to Produce Complex Components From a CAD Solid Model," SPIE Paper No. 2993.
- [17] Kocjan, A., Logar, M., and Shen, Z., 2017, "The Agglomeration, Coalescence and Sliding of Nanoparticles, Leading to the Rapid Sintering of Zirconia Nanoceramics," Scientific Reports, 7, p. 2541.
- [18] Roy, N. K., Foong, C. S., and Cullinan, M. A., 2018, "Effect of Size, Morphology, and Synthesis Method on the Thermal and Sintering Properties of Copper Nanoparticles for Use in Microscale Additive Manufacturing Processes," Addit. Manuf., 21 pp. 17-29.
- [19] Roy, N. K., Dibua, O. G., Jou, W., He, F., Jeong, J., Wang, Y., and Cullinan, M. A., 2017, "A Comprehensive Study of the Sintering of Copper Nanoparticles Using Femtosecond, Nanosecond, and Continuous Wave Lasers," ASME J. Micro Nano-Manuf., 6(1), p. 010903.
- [20] Krebs, F. C., 2009, "Fabrication and Processing of Polymer Solar Cells: A Review of Printing and Coating Techniques," Sol. Energy Mater. Sol. Cells, 93(4), pp. 394-412
- [21] Park, N. G., and Zhu, K., 2020, "Scalable Fabrication and Coating Methods for Perovskite Solar Cells and Solar Modules," Nat. Rev. Mater., 5(5), pp. 333-350
- [22] Hall, D., Underhill, P., and Torkelson, J., 1998, "Spin Coating of Thin and
- Ultrathin Polymer Films," Polym. Eng. Sci., 38(12), pp. 2039–2045.
 [23] Aegerter, M. A., and Mennig, M., S. H., 2004, "Doctor Blade," Sol-Gel Technologies for Glass Producers and Users, Springer Science+Business Media, Berlin, pp. 89-93.
- [24] Suikkola, J., Björninen, T., Mosallaei, M., Kankkunen, T., Iso-Ketola, P., Ukkonen, L., Vanhala, J., and Mäntysalo, M., 2016, "Screen-Printing Fabrication and Characterization of Stretchable Electronics," Scientific Reports., 6, p. 25784.
- [25] Choi, J., Kim, Y.-J., Lee, S., Son, S. U., Ko, H. S., Nguyen, V. D., and Byun, D., 2008, "Drop-on-Demand Printing of Conductive Ink by Electrostatic Field Induced Inkjet Head," Appl. Phys. Lett., 93(19), p. 193508.
- [26] Nayak, L., Mohanty, S., Nayak, S. K., and Ramadoss, A., 2019, "A Review on Inkjet Printing of Nanoparticle Inks for Flexible Electronics," J. Mater. Chem. C, 7(29), pp. 8771–8795
- [27] Kapur, N., Hewson, R., Sleigh, P. A., Summers, J. L., H. M., T., and Abbott, J. S., 2011, "A Review of Gravure Coating Systems," Convert. e-Print, 1(4), pp. 56-60.
- [28] Bariya, M., Shahpar, Z., Park, H., Sun, J., Jung, Y., Gao, W., Nyein, H. Y. Y., Liaw, T. S., Tai, L. C., Ngo, Q. P., Chao, M., Zhao, Y., Hettick, M., Cho, G., and Javey, A., 2018, "Roll-to-Roll Gravure Printed Electrochemical Sensors for Wearable and Medical Devices," ACS Nano, 12(7), pp. 6978–6987.
- [29] Ding, X., and Liu, J., 2016, "Review Article: Transport Phenomena and Fluid Mechanics a Review of the Operating Limits in Slot Die Coating Processes," AIChE J., 62(7), pp. 2508-2524.
- [30] Derjaguin, B., and Landau, L., 1993, "Theory of the Stability of Strongly Charged Lyophobic Sols and of the Adhesion of Strongly Charged Particles in Solutions of Electrolytes," Prog. Surf. Sci., 43(1–4), pp. 30–59.
- Maleki, M., Reyssat, M., Restagno, F., Quéré, D., and Clanet, C., 2011, "Landau-Levich Menisci," J. Colloid Interface Sci., 354(1), pp. 359–363.
 [32] Carvalho, M. S., and Kheshgi, H. S., 2000, "Low-Flow Limit in Slot Coating:
- Theory and Experiments," AIChE J., 46(10), pp. 1907–1917.

 [33] Ruschak, K. J., 1976, "Limiting Flow in a Pre-Metered Coating Device,"
- Chem. Eng. Sci., 31(11), pp. 1057–1060.
 [34] Higgins, B. G., and Scriven, L. E., 1980, "Capillary Pressure and Viscous Pres-
- sure Drop Set Bounds on Coating Bead Operability," Chem. Eng. Sci., 35(3), pp. 673-682.
- [35] Akbarzadeh, V., and Hrymak, A. N., 2016, "Coupled Fluid-Particle Modeling of a Slot Die System," AlChE J., 62(6), pp. 1933–1939. [36] Lin, C., Wang, B., Tiu, C., and Liu, T., 2012, "On the Pinning of
- Downstream Meniscus for Slot Die Coating," Adv. Polym. Technol., 32(2013),
- [37] Behera, D., Roy, N. K., Foong, C. S., and Cullinan, M., 2018, "Nanoparticle Bed Deposition by Slot Die Coating for Microscale Selective Laser Sintering Applications," Proceedings of the 29th Annual International Solid Freeform Fabrication Symposium—An Additive Manufacturing Conference, Austin, TX, pp. 2382-2393.
- [38] Brackbill, J. U., Kothe, D. B., and Zemach, C., 1992, "A Continuum Mehod for Modeling Surface Tension," J. Comput. Phys., 100(2), pp. 335-354.
- [39] Bhamidipati, K. L., Didari, S., and Harris, T. A. L., 2013, "Slot Die Coating of Polybenzimiazole Based Membranes at the Air Engulfment Limit," J. Power Sources, 239, pp. 382-392.
- [40] Didari, S., Ahmad, Z. Y., Veldhorst, J. D., and Harris, T. A. L., 2014, "Wetting Behavior of the Shear Thinning Power Law Fluids," J. Coat. Technol. Res., 11(1), pp. 95-102.
- [41] Ansys, 2017, "Ansys Fluent User's Guide, Release 18.1," Ansys, Canonsburg,
- [42] Ansys, 2017, "Ansys Fluent Theory Guide, Release 18.1," Ansys, Canonsburg,